book

is isotropic press and the other part is viscous stress tensor τ, i.e.

$$\sigma^{\alpha\beta} = -P\delta^{\alpha\beta} + \tau^{\alpha\beta} \tag{3}$$

where $\delta^{\alpha\beta}$ is the Kronecker delta.

For Newtonian fluids, the constitutive equation connecting viscous shear stress and the rate of shear strain are linear. The viscous shear stress is proportional to the rate of shear strain denoted by $\varepsilon^{\alpha\beta}$, which can be expressed as

$$\tau^{\alpha\beta} = \mu\varepsilon^{\alpha\beta} \tag{4}$$

where μ is the dynamic viscosity and

$$\varepsilon^{\alpha\beta} = \frac{\partial v^{\beta}}{\partial x^{\alpha}} + \frac{\partial v^{\alpha}}{\partial x^{\beta}} - \frac{2}{3}(\nabla \cdot v)\delta^{\alpha\beta} \tag{5}$$

The equation of state considers the compressibility of the fluids but ignores the influence of temperature for simplicity. The density of fluid can be written as (Anderson 2002; Tong et al. 2009)

$$\rho = \frac{\rho_0}{K - p/K} = \frac{K\rho_0}{K - p} \tag{6}$$

where K is the bulk modulus of fluid. For water, it usually taken $K = 2.15 \times 109\ N/m^2$, ρ_0 is the fluid density under the condition of standard gas pressure ($\rho_0 = 101325.0$ Pa), and p is fluid pressure.

Accordingly, the pressure can be calculated by density using its changed form

$$p = K(1 - \frac{\rho_0}{\rho}) \tag{7}$$

3 SPH ALGORITHM

The SPH method has been reviewed in details by Randles & Libersky (1996), Liu & Liu (2003, 2010), Monaghan (2005, 2012). In what follows, we just provide a brief introduction of the specific form of SPH model developed in this research for fluid flowing in rough rock fractures, with focuses on treating the rough solid walls and open boundary conditions.

3.1 *SPH discretization*

In SPH method, the computing domain is discretized into a set of disordered integration points or particles. Those particles possess individual material properties, and all the relevant physical quantities (such as density, velocity, energy and etc., depending on the problem) are approximated by the integral representation over neighboring particles. Following above concept, the Navier-Stokes equations can be discretized in the SPH form as (Liu & Liu 2003, 2010)

$$\frac{D\rho_i}{Dt} = \sum_j m_j v_{ij}{}^{\beta} \frac{\partial W_{ij}}{\partial x_i^{\beta}} \tag{8}$$

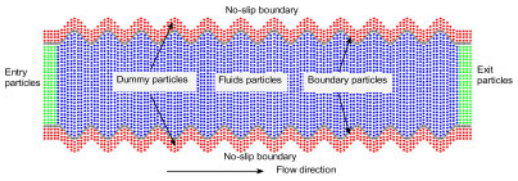

Figure 1. Schematic illustration of solid wall, open boundaries and fluids, dummy particles in the flow region.

$$\frac{Dv_i^{\alpha}}{Dt} = -\sum_j m_j([\frac{p_i}{\rho_i^2} + \frac{p_j}{\rho_j^2})\frac{\partial W_{ij}}{\partial x_i^{\beta}} + \sum_j m_j([\frac{\mu_i \varepsilon_i^{\alpha\beta}}{\rho_i^2} - \frac{\mu_j \varepsilon_j^{\alpha\beta}}{\rho_j^2})\frac{\partial W_{ij}}{\partial x_i^{\beta}} + F_i^{\alpha} \tag{9}$$

where $v_{ij} = v_i - v_j$, m_j, ρ_j denote the mass and density of j-th particle, and the strain of particle i, denoted by $\varepsilon_i^{\alpha\beta}$ can be written in the SPH form as

$$\varepsilon_i^{\alpha\beta} = \sum_{j=1} \frac{m_j}{\rho_j} v_{ji}^{\beta} \frac{\partial W_{ij}}{\partial x_i^{\alpha}} + \sum_{j=1} \frac{m_j}{\rho_j} v_{ji}^{\alpha} \frac{\partial W_{ij}}{\partial x_i^{\beta}} - (\frac{2}{3}\sum_{j=1} \frac{m_j}{\rho_j} v_{ji} \nabla_i W_{ij})\delta^{\alpha\beta} \tag{10}$$

The $\varepsilon_i^{\alpha\beta}$, strain of particle j, can be obtained in a similar way.

3.2 *Kernel function*

The kernel function depends on the smooth length, h, and the non-dimensional distance between particles defined by $R = r/h$, r is the distance between two particles. The Gaussian function, written in Eq. 15, was chosen as the kernel function by its acceptable accuracy and stability performance.

$$W(r,h) = \alpha_D exp\ (-R^2) \tag{11}$$

where the normalized factor α_D is $1/(\pi h^2)$ in 2D and $1/(\pi^{3/2}h^3)$ in 3D.

3.3 *Boundary treatment*

In this research for modeling fluid flowing in rock fractures, two types of boundaries were involved: solid walls and open boundaries including the inflow and outflow conditions (Fig. 1).

3.3.1 *Solid walls*

If rock matrix is supposed to be impermeable, surfaces of rock fractures can be treated by no-slip boundary conditions. In SPH methods, several ways, such as using mirror particles, repulsive force and dummy or image particles are developed to treat the no-slip boundary condition. As reported in Liu & Liu (2003, 2010), the mirror particles method has good performance and efficiency on the smooth planar boundary surfaces. For rough boundary surfaces with complex geometries, it is difficult and time-costing to create

corresponding mirror particles at each time step. Morris et al. (1997) use the fixed image particles to model the curved boundary surfaces, but it still suffers from the particle integral surplus or deficiency at the convex and concave boundary cases (Jones et al. 2010).

In order to treat the boundary surfaces with non-planar geometries due to the roughness of rock fracture surfaces, dummy particles and a repulsive force were adopted to implement the no-slip boundary condition of solid fracture walls. In this method, several layers of dummy particles were fixed on the outside of fracture walls, with same properties of fluids particles, and their pressures, densities and strains were calculated in the same way as that for fluid particles, but their velocities were set by the boundary conditions (for instance, $v_{dummy} = 0$ for no-slip condition, indicating that the location and velocity of dummy particles are not evolved with time, which is convenient for computation). In addition, the number of layers dummy particles was determined by the smooth length of kernel function.

To prevent particles penetrating into the boundary, a repulsive force exerted by the boundary particles on the solid wall is applied when a fluid particles approaching the boundary (Monaghan 1994; Liu & Liu 2003). This repulsive force, denoted by f_{ij}, can be expressed as follow (Monaghan 1994; Liu & Liu 2003, 2010)

$$f_{ij} = \begin{cases} D\left[\left(\frac{r_0}{r_{ij}}\right)^{n_1} - \left(\frac{r_0}{r_{ij}}\right)^{n_2}\right]\frac{x_{ij}}{r_{ij}^2}, & \frac{r_0}{r_{ij}} \le 1 \\ 0 & \frac{r_0}{r_{ij}} > 1 \end{cases} \quad (12)$$

Where the parameters n_1 and n_2 are empirical parameters and usually taken as 12 and 4 respectively (Liu & Liu 2010). D is a constant parameter, taking different values in different problems, usually chosen in the same scale as the square of the largest velocity. The cutoff distance r_0 is usually selected approximately as the initial particle spacing.

3.3.2 *Open boundary conditions*

In most of SPH simulations, open boundaries are implemented using periodic boundary conditions (Liu & Liu 2003) by reinserting the outflow particles (exiting the computational domain) at the inlet boundary and carrying the same properties. This periodic boundary treatment is easy to implement and has a good performance in boundaries of symmetrical geometry, but not valid for rough boundary surfaces with complex and asymmetrical geometry (Hosseini & Feng 2011).

In this paper, for convenient, we just treat all the open boundaries (both inlet and outlet) with Dirichlet boundary conditions, by putting several layers of fluid particles on the upstream (inlet) and downstream (outlet) of the computational domain, named as entry particles and exit particles respectively (seen in Fig.1). Properties of the fluid particles in entry and exit layers were assigned according to the analytical boundary conditions (Hosseini & Feng 2011). In entry layers, all of fluid particles were assigned the prescribed velocities by the analytical solutions, such as that from Poiseuille flow or Cubic law (see Section 4). In the situation of fluid flow in rock fractures, the exit layers represent the outlet boundary, so the velocity of particles in the exit layers can be approximately treated as the same as the fluid particles of the neighboring layer of fluid particles, updated at each time-step.

When a particle of entry layers moves into the computational domain, it becomes an interior fluid particle. Meanwhile, if a particle in the computational domain moves into the exit layer, it becomes an exit particle.

3.4 *Time integration scheme*

The discrete SPH equations can be integrated with standard approaches. In this paper, a two-step Predictor-Corrector scheme (Monaghan 1994), which has second order accuracy in time and better stability, is adapt to calculate the evolution of the primary variables (position, density, and velocity et al.).

For stability, the time-step should be controlled dependent on the force term and the viscous diffusion term which can be expressed respectively as follows (Morris et al. 1997).

$$\Delta t \le 0.25 \min_{\forall j} \left(\frac{h}{f_j}\right)^{1/2} \quad (13)$$

$$\Delta t \le 0.125 \frac{h^2}{\vartheta} \quad (14)$$

In Eqs. 13–14, the parameter h is the smoothing length, f_j is the force acting on the particle $\vartheta = \mu/\rho_0$ is the kinematic viscosity. The minimum of the above conditions is used as the time-step to satisfy all conditions globally.

4 VALIDATION TESTS

In this section, several 2D examples are adapted as benchmarks to validate the SPH method presented above, including the Couette flow and Poiseuille flow (driven by a body force) with analytical series solutions (Morris et al. 1997) and the "parallel plate model" or the "Cubic law" in rock mechanics literatures (Zimmerman 1996; Tong et al. 2010).

4.1 *The Couette flow and Poiseuille flow*

The Couette flow involves a fluid flow between two infinite plates that are initially stationary and located at $y = 0$ and $y = L$. The flow is created by moving the upper plate with a constant velocity v_0 parallel to the x-axis at time $t = 0$. As for Poiseuille flow, it involves a fluid flow between two stationary infinite plates at $y = 0$ and $y = L$. The fluid is initially at rest and is driven by a body force F parallel to the x-axis at time $t = 0$. The analytical series solutions of Couette flow and Poiseuille flow are given by Morris et al. (1997).

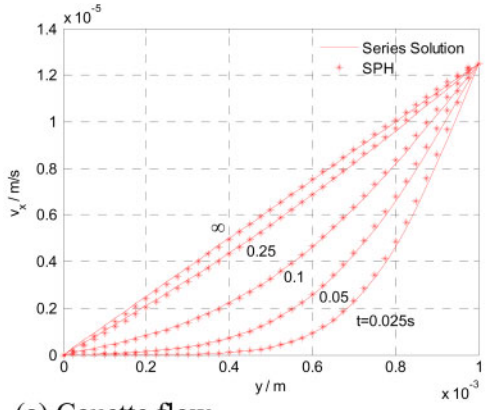

(a) Couette flow

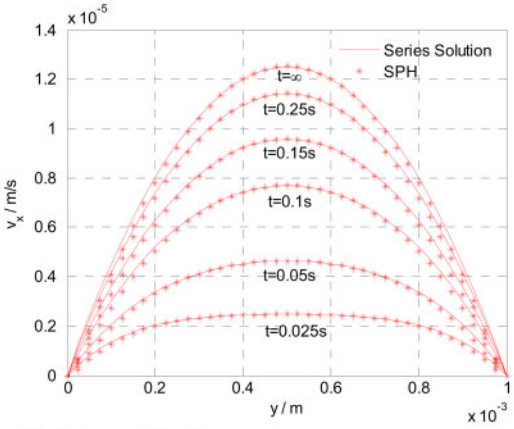

(b) Poiseuille flow

Figure 2. Comparison of SPH simulations with analytical series solutions for Couette flow (a) and Poiseuille flow (b).

For convenient comparison, we chose the model and parameters in our simulations as same as that presented by Morris et al. (1997). It is worth mentioning that in our simulations, the open boundaries, are not treated as periodic boundary conditions as Morris et al. (1997), but treated by aforementioned method in section 3.3. The velocity values in x-axis direction of particles on the line where $x = 0.5$ mm are shown in Fig. 2, as well as the series solutions.

Figure 2 shows a comparison of SPH simulations by our method with the analytical series solutions for the Couette flow and the Poiseuille flow at several times including the steady state ($t = \infty$). The simulated profiles agree well with the analytical series solutions.

4.2 *The parallel plate model*

In the parallel plate model, the pressure and velocity are all zero an the initial time and the flow generated by a hydraulic gradient at the time $t = 0$. In the process of flow, velocities on the upper and lower boundary are zero and the hydraulic gradient keeps constant. Its

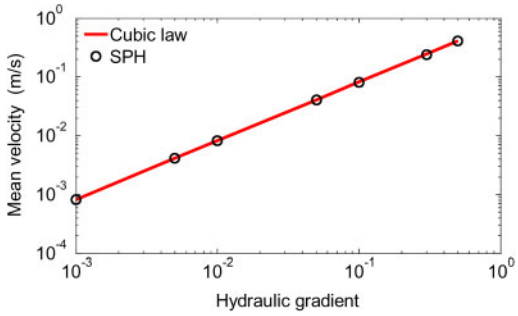

Figure 3. Comparison between theoretic results and SPH simulated results.

solution can be given by the Cubic law expressed as (Zimmerman 1996; Tong et al. 2010)

$$q = \frac{g\rho e^3}{12\mu}\frac{\partial h}{\partial x} \tag{15}$$

where q is the flow rate, $g = 9.8\ \mathrm{m/s^2}$ is the gravitational accelerate coefficient, ρ is the density of fluid, e is the distance (aperture) between the parallel plates, μ is the viscosity of fluid, and $\partial h/\partial x$ is hydraulic gradient or mean hydraulic gradient.

Then the mean velocity can be expressed as

$$\bar{v} = \frac{g\rho e^2}{12\mu}\frac{\partial h}{\partial x} \tag{16}$$

In our SPH simulations, the geometry of parallel plate model is 5mm in the length of parallel surfaces and 1mm in the width between two plates. The smoothing length is 1.1times of initial particle spacing (0.025 mm). Seven sets of hydraulic gradient $\partial h/\partial x = 0.001, 0.0005, 0.01, 0.05, 0.1, 0.5$) were simulated. Their mean velocities when they reached the steady state (about 10000 time-steps, each time-step is 1×10^{-5} s) at the location of $x = 2.5$ mm are plotted and compared with the theoretic solutions given by Cubic law by Eq. 16 in the Fig. 4.

As can be seen from Fig. 4, at different hydraulic gradients, the mean velocities solved by SPH match very well with the Cubic law solutions. That is to say, the boundary treatment approaches in our simulation have sufficient effectiveness and accuracy.

5 FLUID FLOW IN SINGLE FRACTURES AND FRACTURE INTERSECTIONS

To investigate the fluid flow process in single fracture and intersected fractures, a simplified single curvilinear fracture model (with varying aperture) and two intersected fractures models (geometrical symmetry and asymmetry) were studied, and the results are reported and compared with Cubic law derived from Reynolds equation.

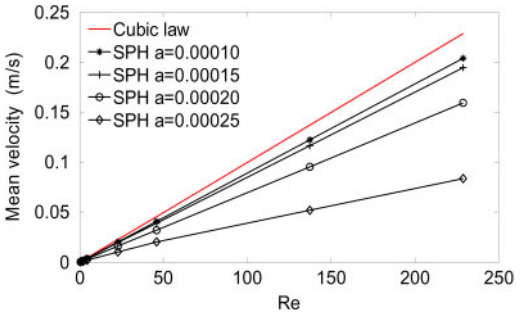

Figure 4. Comparison between Cubic law and SPH simulated results.

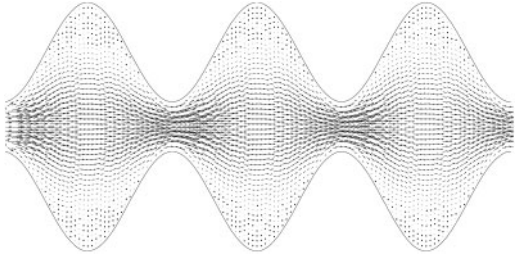

Figure 5. Distribution of velocity vectors (Re = 230).

5.1 *Fluid flow through a fracture of varying aperture*

In this simulation, we studied a simplified fracture with varying aperture. The length of fracture is 3 mm ($x \in [0\ \ 0.003]$), and the y coordinate of lower surface is given by Eq. (17a), and the y coordinate of upper surface is decided by Eq. (17b)

$$y_{lower} = a\,cos(2000\pi x + 0.00025) \tag{17a}$$

$$y_{upper} = -y_{lower} + 0.00075 \tag{17b}$$

where the parameter a controls the roughness ranges of the varying aperture.

Figure 4 shows the comparison between the SPH simulated mean velocity under different values of a and theoretic mean velocity calculated by using the Cubic law at different Reynolds numbers defined as $Re = \vec{V}L/v$, where $\vec{V}$ is the mean velocity along the flow direction, L is the mean width of fracture and L is the kinematic viscosity of fluid.

Apparently, the relationship between mean velocity and the Reynolds number are still linear in general when the parameter a was changed, and the SPH models results have more significant discrepancies with the theoretic solution by using the Cubic law when the Reynolds number increasing, indicating the invalidity of the Cubic law in such situations. From the results under different value of parameter a, it can be found that even such a simply and slight change of the shape of surface causes decrease of its mean velocity, not only because of the increase of boundary of

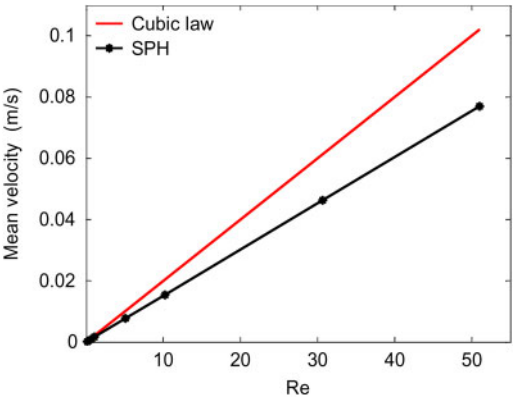

Figure 6. Comparison between Cubic law and SPH results.

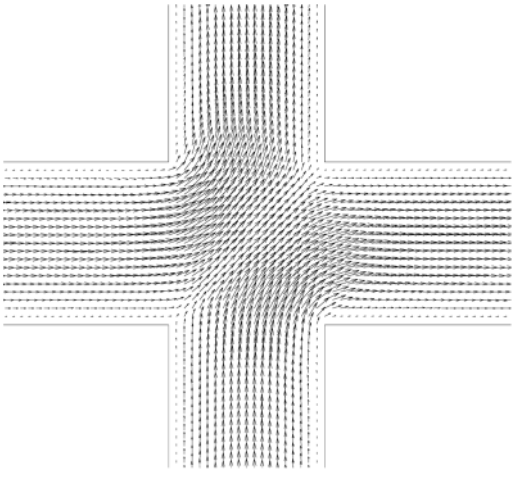

Figure 7. Distribution of velocity vectors (Re = 50).

fluid flow, but also because of the decrease of effective aperture that was predicted by SPH model solving Navier-Stokes equations.

Figure 5 presents the distribution of fluid velocity vectors in this case. Apparently, because of the shear resistance on the boundary, the fluid velocities in the areas of peaks are much smaller than the velocity in the middle narrow regions. The much increased area of the rough boundary surfaces reduced the overall effective aperture and velocity of fluid flow, which is difficult for modeling using Cubic law.

5.2 *Fluid flow in orthogonal intersection*

Fracture intersections are the basic elements of fracture network models in rock mechanics. In this section, the simplest one, orthogonal intersection is simulated. In this simulation, the width of fracture is 0.5 mm and the length of each branch (right, left, up and down) is 1 mm. The left and down branch are the inlet of flow, and the right and up branch is the outlet of flow. For keep the symmetry, the initial velocity of inlet is the same.

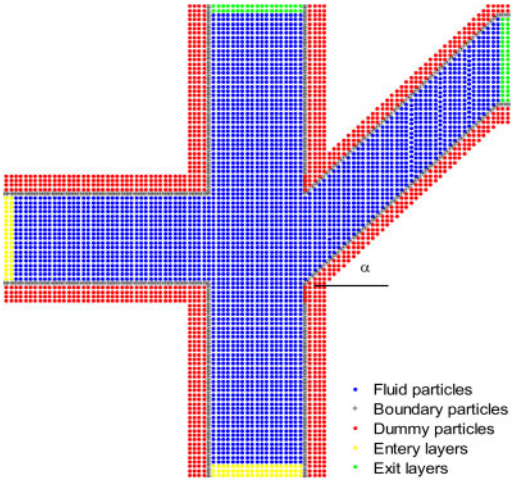

Figure 8. Discretized model of asymmetry intersections ($\alpha = 45°$).

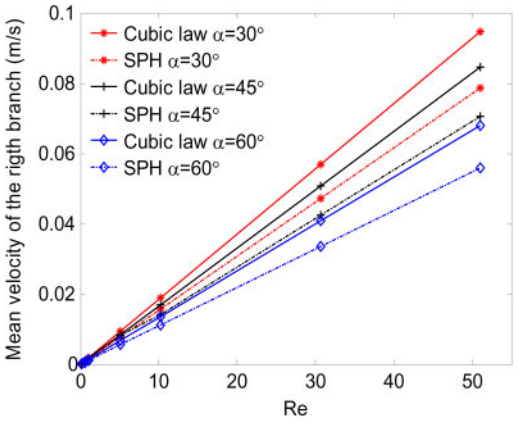

Figure 9. Comparison between Cubic law and SPH results.

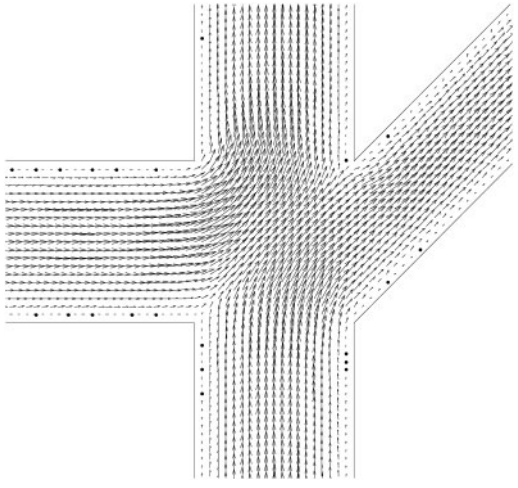

Figure 10. Distribution of velocity vectors ($\mathrm{Re} = 50$, $\alpha = 45°$).

Seven sets of simulations with different inflow velocities were studied. Fig. 6 shows the comparison of the results of SPH simulations with the solution by using the Cubic law. When the Reynolds number is around 1.0, the results show good agreement between SPH models and models using the Cubic law. With the increase of Reynolds number, although the relationship of mean velocity of outflow branch and the Reynolds number is still linear in general, the difference between results of SPH models and models using the Cubic law solution becomes more significant, indicating increasing invalidity of the Cubic law with increasing values of the Reynolds number, for fluid flow at fracture intersections with geometrical symmetry.

Figure 7 presents the distribution of velocity vectors in the intersection. It can be seen that the velocity vectors also keep symmetry because of the symmetry of geometry and inflow velocity.

5.3 *Fluid flow in asymmetry intersections*

To study the behavior of flow in the asymmetry intersections, we let the right branch of fracture intersection model rotate a degree of α. The model can be seen in Fig. 8. Three models, with the α value equal to 30°, 45° and 60° respectively, were simulated, and the results were plot in Fig. 9. The mean velocity of the rotated branch (right branch) reduces with the α increasing because of the reducing effective aperture of this branch. Similar with the orthogonal intersection, with the increase of Reynolds numbers, the mean velocity of outflow branch simulated by SPH have an obvious decrease compared with the solution of models using the Cubic law.

Figure 10 shows the distribution of velocity vectors when the α is 45° and the Reynolds number is 50. The flow is divided in the intersect part, with much more fluids flowing in the up branch than that through the right branch.

6 CONCLUSION

The conclusions of this study can be summarized as follows.

According to the result of benchmark tests, the SPH models and the boundary treatment methods proposed in this paper are effective and have acceptable accuracy.

The roughness of fractures surface have an obvious impact upon the velocity of fluid flow because the roughness not only increased the boundary areas of flow, but also reduced the effective apertures of the fractures. This effect can be represented in a straightforward way by SPH model of Navier-Stokes equation,

but remains a challenge for models using much simplified Reynolds equation and the Cubic law of rock fractures.

In our simulation, although the relationship between the mean velocity and Reynolds number are still linear both in single fractures and intersections, due to the relatively small values of the Reynolds number we adopted, the results indicate that models using the Cubic law derived from Reynolds equation overestimate the mean velocity of the fluid flow in fractures even with such smooth but curved fractures. Such overestimation might also increase if more realistic roughness of fracture surfaces need to be considered and could lead to certain underestimation of the travel time of solute transport in fractured crystalline rocks, which may induce unknown uncertainties for realistic modeling of the mass transport processes.

REFERENCES

Hosseini, S.M. & Feng, J.J. 2011. Pressure boundary conditions for computing incompressible flows with SPH. Journal of Computational physics. 230:7473-7487.

Jones, V., Yang, Q. & McCue-Weil, L. 2010. SPH boundary defi-ciency correction for improved boundary conditions an de-formable surfaces. Ship Science & Technology. 4:21–30.

Koyama, T., Neretnieks, I. & Jing, L. 2008. Anumerical study on difference in using Navier-Stokes and Reynolds equations for modeling the fluid flow and particle transport in single rock fractures with shear. Int. J. Rock Mech. Min Sci., 45:1082–1101.

Liu, G.R. & Liu, M.B. 2003. Smoothed particle hydrodynamics: a meshfree particle method. World Scientific, Singapore.

Liu, M.B. & Liu, G.R., 2010. Smoothed particle hydrodynamics (SPH): an overview and recent developments, Archives of Computational Methods in Engineering. 17:25–76.

Morris, J.P., Fox, P.J., & Zhu, Y. 1997. Modeling low Reynolds number incompressible flows using SPH. Journal of Computational Physics. 136:214–226.

Monaghan, J.J. 1994. Simulating free surface flows with SPH, J. Comput. Phys. 110:399–406.

Monaghan, J.J.2012. Smoothed Particle Hydrodynamics and Its Diverse Applications. Annu. Rev. Fluid Mech. 44: 323–46

Randles, P.W. & Libersky, L.D. 1996. Smoothed Particle Hydro-dynamics: Some recent improvements and applications. Computer Methods in Applied Mechanics and Engineering. 139:375–408

Tong, F, Jing, L. & Zimmerman, R.W. 2009. A numerical study of vis-cous fluid flow in a single fracture. New development in rock mechanics and engineering. In: Proceedings Conference on New Direction in Rock Mechanics, Liberty Culture & Technology, pp165–170.

Yeo, I.W. & Ge, S. 2005. Applicable range of the Reynolds equa-tion for fluid flow in a rock fracture. Geosciences Journal. 9(4):347–352.

Zimmerman R.W. & Bodvarsson G.S. 1996. Hydraulic conductivity of rock fractures, Transport in Porous Media 1996, 23:1–30.